An empirical potential for simulating hydrogen isotope retention in highly irradiated tungsten

OPEN ACCESS
IOP Publishing
Journal of Physics: Condensed Matter
J. Phys.: Condens. Matter **35** (2023) 495901 (17pp)
https://doi.org/10.1088/1361-648X/acf25f

An empirical potential for simulating hydrogen isotope retention in highly irradiated tungsten

Daniel R Mason[1,*], Duc Nguyen-Manh[1], Victor W Lindblad[2], Fredric G Granberg[2] and Mikhail Yu Lavrentiev[1]

[1] UK Atomic Energy Authority, Culham Centre for Fusion Energy, Oxfordshire OX14 3DB, United Kingdom
[2] Department of Physics, University of Helsinki, PO Box 43, Helsinki FIN-00014, Finland

E-mail: daniel.mason@ukaea.uk

Received 2 May 2023, revised 29 June 2023
Accepted for publication 21 August 2023
Published 8 September 2023

Abstract

We describe the parameterization of a tungsten-hydrogen empirical potential designed for use with large-scale molecular dynamics simulations of highly irradiated tungsten containing hydrogen isotope atoms, and report test results. Particular attention has been paid to getting good elastic properties, including the relaxation volumes of small defect clusters, and to the interaction energy between hydrogen isotopes and typical irradiation-induced defects in tungsten. We conclude that the energy ordering of defects changes with the ratio of H atoms to point defects, indicating that this potential is suitable for exploring mechanisms of trap mutation, including vacancy loop to plate-like void transformations.

Keywords: hydrogen isotope, fusion materials, lattice defects, tungsten, interatomic potential

(Some figures may appear in colour only in the online journal)

1. Introduction

For viable commercial D-T nuclear fusion, it is essential that the breeding of tritium at least balances the tritium which is retained after having penetrated the components. One of the critical reactor components requiring study in this regard is the tungsten divertor, which is anticipated to undergo very high neutron flux [1, 2] and so develop a highly damaged microstructure, especially near coolant pipes where the temperature is kept below the onset of stage III recovery (vacancy migration) [3–6]. It is well established that irradiation-induced lattice defects within tungsten act as strong traps for hydrogen isotopes [7–12]. While the modelling of binding energies of hydrogen to prototypical small defects is properly undertaken by density functional calculations, there is an emerging awareness that in the high irradiation dose limit the complex defect microstructure both generates and is responsive to stress [13, 14]. This in turn can influence the evolution of defects [15, 16] and lead to defect stabilization [17–21]. Such complex emergent mechanisms require very large molecular dynamics simulations which in turn requires simple empirical potentials [22, 23].

Here, we develop a new potential for tungsten-hydrogen based on the embedded atom model, specifically designed for use with simulating high dose irradiation. It is only reasonable to expect an empirical potential to correctly reproduce the properties included in the set used during development, and so over time, as a new set of properties become of interest, it becomes necessary to develop or refine potentials.

* Author to whom any correspondence should be addressed.

We conclude that the bond-order potentials of Li *et al* [24] and Juslin and Wirth [25] have unsatisfactory binding energy of H atoms to a monovacancy, thought to be the most important factor in understanding hydrogen-isotope retention at high dose [26]. This is remedied by the EAM potentials by Bonny *et al* [27] and Wang *et al* [28], but all these potentials have poor vacancy-cluster binding, hydrogen-to-surface binding, and surface energies, making them difficult to rely on for simulating larger clusters [29, 30], for correctly predicting the energy ordering of void-like and vacancy-loop defects [31, 32], or spontaneous bubble formation [33].

Our principle point of comparison for the correct behaviour of our potential is electronic structure density functional theory (DFT) calculations. In this work we report some new DFT calculations performed to find the relaxation volumes of vacancy-hydrogen clusters. The accurate prediction of relaxation volumes for various induced defects using DFT calculations plays an important role in understanding lattice swelling and trapping mechanisms in materials under irradiation within the multi-scale modelling approach [10, 34–38], and this work specifically aims to reproduce these properties with an empirical potential. We make extensive comparison to the empirical potential of Wang *et al* [28], which we believe gives the best values in the current literature for hydrogen-vacancy cluster binding energies.

In section 2.1, we show that the monovacancy and vacancy cluster properties in pure tungsten match DFT results, including the low divacancy binding energy [39], vacancy migration barriers, and relaxation volumes. In section 2.4, we show the binding energies of H atoms to vacancies and interstitials, and relaxation volumes of vacancy-H clusters also match DFT results. We also find an increased binding of the H atom to the surface compared to previous work. We show that molecular hydrogen is stable inside voids, and that increasing the H/point defect ratio increases the stability of open vacancy structures. Finally in section 3, we compute properties for lattice defects typical of irradiation damage—small dislocation loops and voids. We show that molecular H_2 exists within nanocavities, and that a supersaturation of hydrogen gas atoms can significantly disrupt the local atomic structure around dislocation loops in order to reduce energy.

Throughout this work we have made comparisons excluding the zero point energy contributions to the binding energy, which are not insignificant for hydrogen isotopes. This choice has been made to avoid fitting the classical potential energy surface to the curvature of the potential energy found in DFT. This is also an acknowledgement of the fact that molecular dynamics (MD) simulations are classical, and so do not include quantum-mechanical phonon effects. We have, however, computed zero point energy corrections for this potential and added these to the results separately as appropriate. We have also decided to compute and report relaxed zero temperature defect configurations rather than dynamic effects at elevated temperatures, leaving this to future work. A limited number of dynamic properties of the tungsten lattice are given in section 2.2.

This empirical potential is well suited to simulations of the retention of deuterium in highly irradiated tungsten [40], and to investigate trap mutation mechanisms whose effect is clear experimentally [41, 42] but where the atomistic origin is currently speculation.

1.1. The form of the potential

The basic form of the embedded atom potential suggested by Daw and Baskes [43] gives the potential energy E_i of atom i as a local function of the positions and types of the neighbouring atoms. We write the distance from atom i to a neighbour j as x_{ij}, and the types of atoms i and j as α and β respectively. Then

$$E_i = \frac{1}{2}\sum_j V_{\alpha\beta}\left(x_{ij}\right) + F_\alpha\left(\sum_j \phi_\beta\left(x_{ij}\right)\right), \qquad (1)$$

where $V_{\alpha\beta}(x)$ is a pairwise interaction energy depending on the type of both atoms, $\phi_\alpha\left(x\right)$ is an electron density function, depending only on the type of the neighbour, and $F_\alpha(\rho)$ is an embedding function capturing the many-body nature of metallic bonding. This potential form for alloys is supported by the classical MD code `LAMMPS` [44] as the `eam/alloy` pair style.

We have made changes to the forms of the functions V, ϕ, and F, suggested by Finnis and Sinclair [45] and later developed by others for similar potentials. The first observation we make is that potential hardening at short range is often required to simulate displacement cascades [25, 46–48]. Typically the short-range hardening used is the universal ZBL form [49] added as a very large correction at short range. Here we start with the ZBL form for the pairwise interaction V_α, and add a small correction near equilibrium lengths. Secondly, we note that in the second moment approximation, the embedding function $F_\alpha[\rho]$ has a square root form [50], which is very successful for modelling transition metals. We add a spline correction to this function. The final observation we make is that potentials need to be smooth in their second derivatives at least in order to avoid discontinuities in the quasiharmonic phonon spectrum. We ensure this by using quintic splines with well-separated knots. The explicit form of the potential, and all the parameters needed to reconstruct a data-table is given in the appendix.

2. Fitting the potential

The three parts of the potential, giving the W–W, H–H and W–H interactions, were fitted separately, then together, to reproduce sets of electronic-structure derived data. Possible fits to the target data set were then run through an expanded set of more time-consuming tests, reported here, to check for transferability. We report the overall best performing parameterization.

Table 1. Targetted properties of the W–W potential. A comparison is given to the empirical EAM form 'EAM-2' [51], and a our earlier MNB potential [36].

Category	Property	Units	DFT	Expt	This work	EAM-2	MNB
perfect	lattice const	Å	3.186[a]	3.1652[b]	3.145	3.140	3.1652
bcc	cohesive energy	eV		8.90[b]	8.949	8.900	8.900
lattice	C_{11}	eV Å^{-3}	3.229[a]	3.324[c]	3.201	3.260	3.222
	C_{12}	eV Å^{-3}	1.224[a]	1.279[c]	1.257	1.265	1.263
	C_{44}	eV Å^{-3}	0.888[a]	1.018[c]	1.020	0.996	0.998
point	E_f^v	eV	3.619[d]		3.631	3.49	3.727
defects	$\Omega_{\rm rel}^v$	Ω_0	−0.32[a]		−0.329	*−0.045*	−0.36
	E_m^v	eV	1.756[d]		1.754	1.856	1.523
	V_2 binding	eV	0.048[d]		0.080	*0.490*	0.170
	V_3 binding	eV	0.311[d]		0.365	*1.417*	0.433
	$E_f^i([111])$	eV	10.5		9.736	10.52	9.31
	$\Omega_{\rm rel}^i$	Ω_0	1.57[a]		1.485	*1.172*	1.40
	$E_f^i([100]) - E_f^i([111])$	eV	0.29		0.236	0.30	0.25
surface	$E_{\{110\}}$	eV Å^{-2}	0.212		0.220	*0.144*	0.218
energy	$E_{\{100\}} - E_{\{110\}}$	eV Å^{-2}	0.047		*0.028*	*0.026*	*0.021*

[a] Mason *et al* [54].
[b] Finnis and Sinclair [45].
[c] Featherston and Neighbours [55].
[d] Mason *et al* [36].
In this table and subsequently, italics indicate values which could produce significant errors in simulation. These values are discussed in the text.

2.1. W–W properties

The W–W potential was fitted to structural and elastic properties of bcc tungsten, to vacancy cluster properties and surface formation energies, and to single interstitial properties. The initial fit was chosen to be as close as possible to the MNB potential [36]—a modification of the transferable Finnis–Sinclair form with improved vacancy cluster properties—within the constraints of the new functional form. The downhill simplex method was used to minimise the fitting in a least-squares sense. Additional weighting was placed on keeping the knot points in the potential far apart, in order to mitigate overfitting. The fitted properties are given in table 1, and include formation energies (denoted E_f in the text and tables), relaxation volumes ($\Omega_{\rm rel}$), binding energies (E_b), and migration energies (E_m) for point defects. A comparison is given to two empirical EAM forms: 'EAM-2' given by Marinica *et al* [51], as this is the basis for the W–W part of both the Bonny *et al* [27] and Wang *et al* [28] W–H potentials; and our earlier MNB potential [36]. We find that the potential described here is good in these targetted properties, as indeed are the comparison potentials generally. A direct comparison between the functional forms for this work and the EAM-2 potential [51] is shown in figure 1. The only significant difference to the eye is that this work has a shorter range—the EAM-2 potential has a long range repulsion between equilibrium atom spacings which has a strong effect on the energetics of interstitial defects.

We first consider vacancy and open surface properties. The new potential performs comparably to the MNB in the vacancy cluster and surface energy properties, which was itself designed to improve on the EAM-2 results. The only significant improvement we make in this redraft of the W–W part of the potential is a better monovacancy migration energy, which was included in the refitting. We find with a nudged elastic band calculation that this is raised from 1.52 eV in MNB to 1.75 eV in this work, which can be compared to the DFT value 1.75 eV [36]. This result is illustrated in figure 2(a).

The divacancy energies and migration barriers are also a good fit to the DFT values of [36]. If one vacancy is at lattice site [0 0 0], the lowest energy configuration is with the second vacancy at nearest neighbour [$^1/_2$ $^1/_2$ $^1/_2$], though even here the binding energy is only 0.080 eV. To move the second vacancy to position [1 0 0], [1 1 0], [1 1 1] has a barrier 1.900, 2.146, 1.696 eV respectively, which can be compared to the pattern of the DFT values 1.825, 1.807, 1.717 eV [36]. The trivacancy binding energy is reproduced well, but its migration barrier is not. This potential finds the migration barrier 1.752 eV, similar to that of the monovacancy. But DFT is able to rehybridise the electrons at the saddle point configuration, and finds a low saddle point of 1.146 eV. This problem with EAM empirical potentials was discussed in [36].

We define the formation and binding energies of a m—vacancy cluster in tungsten as, respectively,

$$E_f^{v_m} = E(v_m) - (N-m)E_0$$
$$E_b^{v_m} = mE_f^{v_1} - E_f^{v_m}, \qquad (2)$$

where $E(v_m)$ is the lowest total energy of a box containing N lattice sites of which m are vacant, and E_0 is the energy per tungsten atom (equal to the negative of the cohesive energy). For this work, the lowest energy has been found in the same manner as [36]. m sites were selected as a string of nearest neighbour positions, within a box of $7 \times 7 \times 7$ conventional unit cells, removing the atoms on those sites, and relaxing

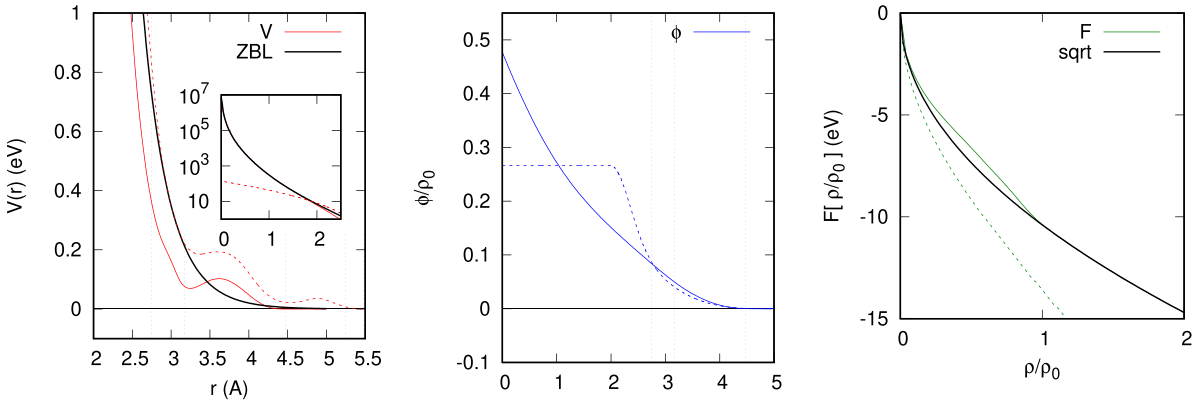

Figure 1. W–W potential comparison to [51] (dashed lines). (a) Pairwise potential, black line ZBL repulsion. (b) Density function, (c) embedding function, black line square root form. The vertical lines in (a) and (b) indicates the equilibrium spacing of neighbours in the bcc lattice. The density is scaled in (b) and (c) by the level for a W atom in the perfect bcc lattice.

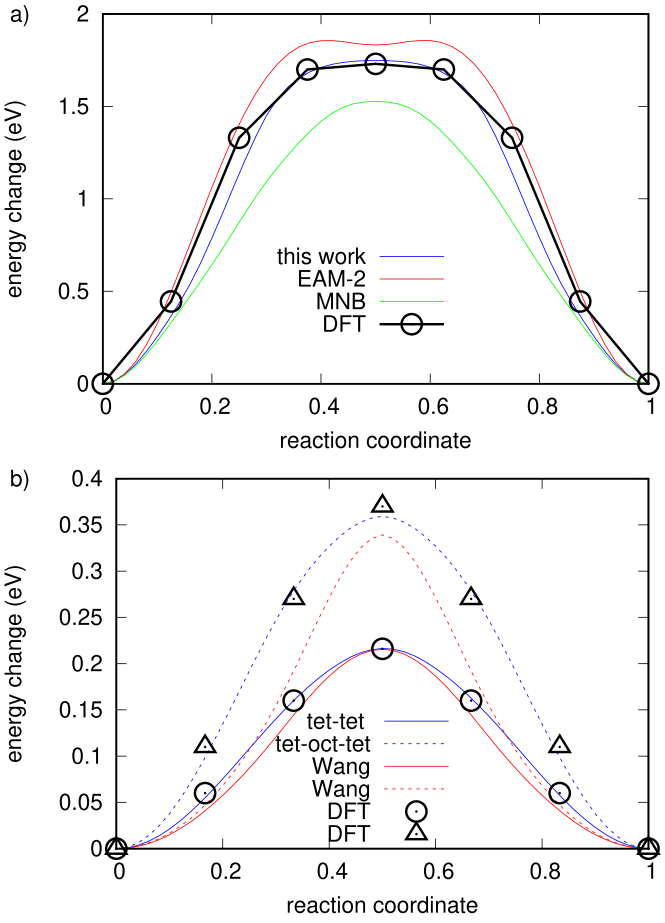

Figure 2. NEB calculation for migration in W. (a) Monovacancy migration, compared to DFT result from [52], with lines to guide the eye. (b) H in otherwise pure W. DFT comparison results from Kong *et al* [53].

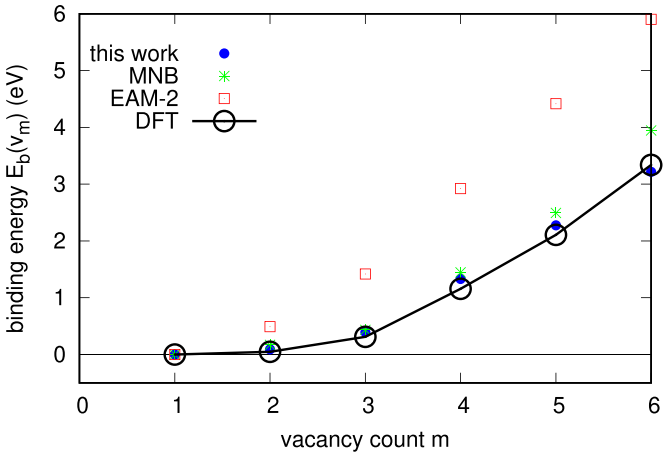

Figure 3. (Total) binding energy of vacancy clusters in pure tungsten.

atomic positions with constant volume. Up to one thousand randomly selected strings of atoms were compared to find a good minimum energy configuration. The relaxed energy quoted includes an elastic energy correction [56].

The binding energy of vacancy clusters in pure W is shown in figure 3, and relaxation volumes of vacancy clusters are shown in figure 4(a). We see that the current potential finds excellent agreement with DFT values from [36], a slight improvement on the previous MNB potential and a considerable improvement on the EAM-2 potential.

The properties of some unreconstructed low index surfaces in pure W are given in table 2. The surface energies and stresses are a good match to DFT results from [57]. As noted in [36], the high formation energy of the surfaces in bcc tungsten is due to the pseudo-gap in the electronic density of states near the Fermi level—the practical outcome of which is to make electron-deficient tungsten atoms higher energy than the square-root form of the embedding function second-moment (Finnis–Sinclair) potentials would suggest. The approximate energy level of the surfaces is therefore adjusted by reducing the embedding energy in this low-electron-density region, as can be seen in figure 1(c). We note that the energy of the [1 0 0] surface is lower than the [1 1 1] surface, in common with other empirical EAM or tight-binding

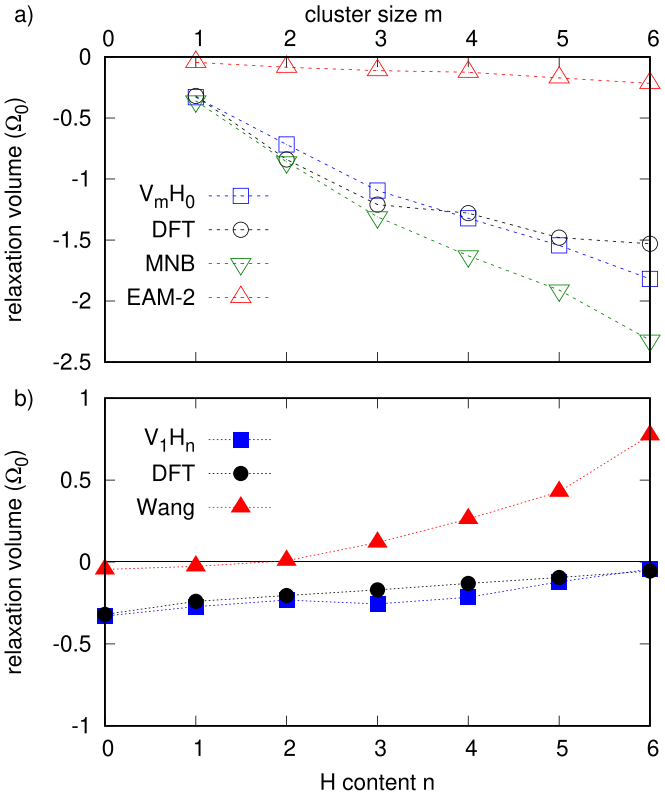

Figure 4. Relaxation volumes of (a) empty vacancy clusters V_m and (b) monovacancies filled with H V_1H_n, in units of the atomic volume Ω_0. The lines are to guide the eye. DFT results in figure (a) from [36].

Table 2. Surface properties of the W potential. Surface energies γ_{hkl} and surface stresses s_{hkl} for surface normal $[hkl]$ are given in eV Å^{-2}. DFT and MNB values from [57], experiment from [59]. Values showing significant discrepancy are indicated with italics.

Property	DFT	Expt	This work	EAM-2	MNB
γ_{110}	0.212	0.229	0.220	*0.144*	0.218
γ_{211}	0.224		0.248	*0.171*	0.241
γ_{111}	0.239		0.266	*0.184*	0.259
γ_{100}	0.259		0.248	*0.170*	0.240
s_{110}	0.301, 0.178		0.363, 0.194		0.330, 0.215
s_{211}	0.223, 0.151		0.220, 0.151		0.262, 0.251
s_{111}	0.135, 0.135		0.130, 0.130		0.215, 0.215
s_{100}	0.147, 0.147		*0.242*, *0.242*		*0.229*, *0.229*

second-moment approximation (Finnis–Sinclair) potentials. In these potentials, the leading energy contribution can be estimated by simply counting bonds: the surfaces (1 1 0), (2 1 1), (1 0 0) and (1 1 1) have, respectively a nearest- and next-nearest- neighbour count of (6,4), (5,3), (4,5), and (4,3). Hence the (1 1 0) surface has the lowest energy, in qualitative agreement with DFT calculations, but the (1 1 1) surface has the highest energy. However the empirical potential models that relate the surface energies to the cohesive energies are flawed because while they include the contributions from the d band in transition metals, they ignore the general trend

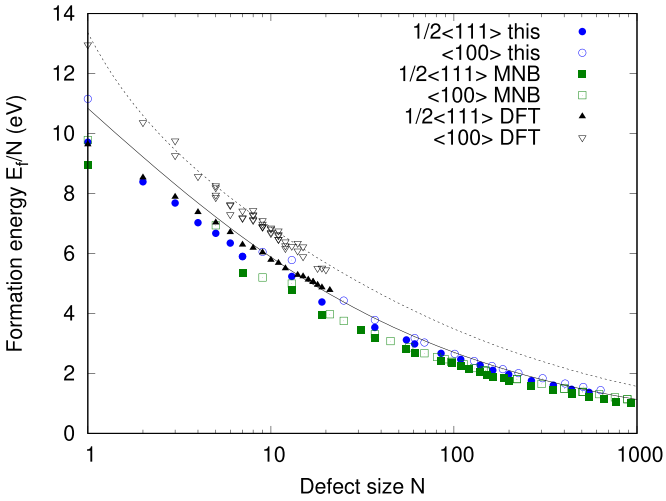

Figure 5. Formation energy of interstitial clusters and loops per point defect. DFT results from [60], with extrapolating lines being fits to the data from [54].

of sp electrons to spread smoothly at the surface. The latter sp-d hybridisation not only affects the attractive bonding contributions but also the repulsive energy from electrostatic and exchange-correlation contributions. Using DFT calculations, the predicted surface energies can be improved by 10%–20% leading to the different trends observed [58].

The practical result of this failing of EAM potentials is that the (1 0 0) surface is the least reliable, and both the surface energy and surface stress are not well reproduced.

We now consider interstitial properties of the W–W potential. Interstitial properties were computed in a $5 \times 5 \times 5$ conventional unit cell with fixed volume and the elastic correction made, to be a close comparison to DFT values. The formation energies for single interstitials in $^1/_2[1\,1\,1]$ and [1 0 0] orientations are raised slightly compared to the previous MNB potential, which we have achieved by adding a small repulsive bump in the pairwise potential $V(r)$ between second- and third- neighbour positions, similar to the one seen in EAM-2. The relaxation volume of the $^1/_2[1\,1\,1]$ crowdion is found to be 1.485 times the volume per tungsten atom in the perfect 0 K lattice, Ω_0. This is a good match to the DFT—determined relaxation volume, 1.57 Ω_0 [54].

The transferability of the potential to larger interstitial clusters is tested by computing the formation energy of interstitial clusters and loops in pure W, shown in figure 5. Small interstitial clusters up to size 6 point defects were generated using a method similar to vacancy clusters, constructing a string of m lattice sites at random, then placing an interstitial atom into randomly selected tetrahedral or octahedral sites along the string. 500 such strings were constructed to find a low energy, using a cell size $16 \times 16 \times 16$ unit cells with fixed volume. Larger interstitial loops were constructed to be circular within a box size $48 \times 48 \times 48$ unit cells with fixed volume. The energy per point defect is slightly higher than in the MNB or AT potentials, and the increase in energy of [1 0 0]—Burgers vector defects over those with

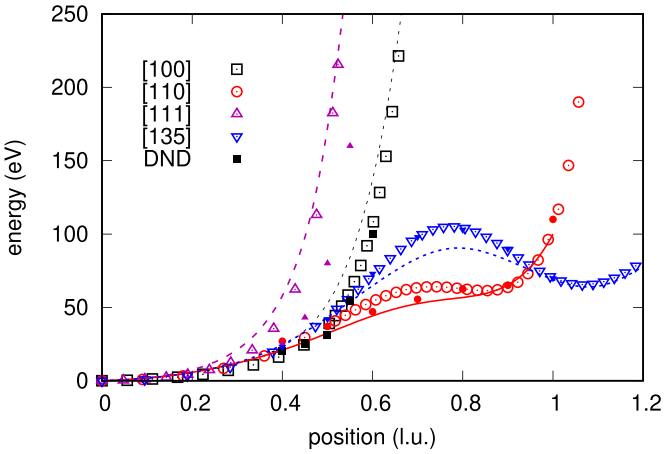

Figure 6. Energy for quasi-static drag of a single atom in direction indicated. Lines denote DFT values from [48]. Some representative points for the DND interatomic potential from [48] are shown using filled symbols.

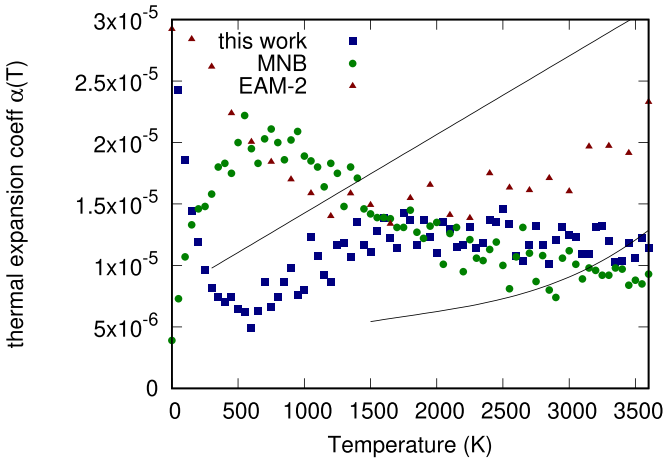

Figure 7. Thermal expansion coefficient, defined by $\Delta L/L = \alpha(T)\Delta T$ of pure tungsten crystal as computed using MD in the NPT ensemble. Experimental results: upper line Miiller and Cezairliyan [65], lower line Dubrovinsky and Saxena [66].

$^1/_2$[1 1 1] is raised slightly. A comparison to DFT [54, 60] shows both these changes are improvements, and in particular the $^1/_2$[1 1 1] loops are in good agreement with DFT. We note that the GAP potential of [61] is closer to DFT for the [1 0 0] loops. Some other tungsten empirical potentials [51, 62] find [1 0 0] loops have the lower energy. While the significance of this ordering is not clear in atomistic high dose microstructures generated by MD [22, 23, 63], we shall see in section 2.4 that the energy ordering of dislocation loops is further affected by the presence of hydrogen isotopes, so these potentials cannot be used as a base for seeking trap mutation mechanisms depending on defect energy ordering.

We consider the transferability of the short-range part of the W–W potential using the Quasi-Static Drag (QSD) method introduced by Becquart *et al* [48]. A single atom is displaced along a fixed vector direction, and the energy is recorded without relaxing the atoms. We consider vector directions [1 0 0], [1 1 0], [1 1 1], [1 3 5]. As the atoms get close together, the potential tends to the ZBL repulsive form, and the energy rises rapidly. The results are shown in figure 6. DFT results generated in [48] using semi-core electrons in the PAW approximation are indicated in the figure, and we see this work follows the DFT values quantitatively for the head-on collisions considered ([1 0 0] and [1 1 1]), and is acceptable for the [1 1 0] and [1 3 5] directions. To make a proper comparison with literature, we include indicative results generated using the DND W potential [62], known to generate collision cascades in agreement with experimental observations [64]. We see this work is very similar to DND, closer than the other empirical potentials considered in [48], but we note that this work follows DFT more closely even than DND for the head-on [1 1 1] collision.

2.2. *Dynamic properties of the tungsten crystal*

In this section we compute some simple dynamic properties of the pure tungsten crystal, in order to demonstrate the stability at elevated temperatures. No phonon properties were included in the fitting, so these results represent a test of transferability to MD simulation.

Figure 7 shows the thermal expansion coefficient of pure tungsten crystal computed using molecular dynamics in the NPT ensemble using PARCAS [67, 68]. Comparing to experimental results shows that all potentials considered here give good thermal expansion properties above room temperature, with this work and EAM2 starting from a slightly lower lattice constant at 0 K. The melting points for MNB and this work were found using the two-phase method [69] to be 5050 ± 50 K and 4950 ± 50 K respectively. These values are high compared to experiment (3695 K), a common failing of empirical potentials [14].

Figure 8 shows some phonon properties of the perfect tungsten crystal. These plots were generated at 0 K using the ideal lattice parameter by direct diagonalization of the dynamical matrix [71]. This work behaves similarly to the MNB potential, which is a fair match to the experimental phonon dispersion relation and density of states. The low-frequency density of states shows the quadratic rise characteristic of the Debye model. As the speed of sound is very similar in all the empirical potentials considered, and set to be close to experiment [70], the curves overlap at low frequency. The first peak, corresponding to transverse-mode phonons is at a slightly lower frequency than experiment in the MNB potential and this work, and the second peak (longitudinal phonons) is higher frequency than experiment. The EAM-2 potential shows phonon properties characteristic of bcc metals, but with both peaks significantly below experimental values. We find the maximum phonon frequency in this model is 7.62 THz, compared to 6.6 THz experimentally [70]. A value around 6 THz is commonly taken as a characteristic frequency in object kinetic Monte Carlo simulation [72].

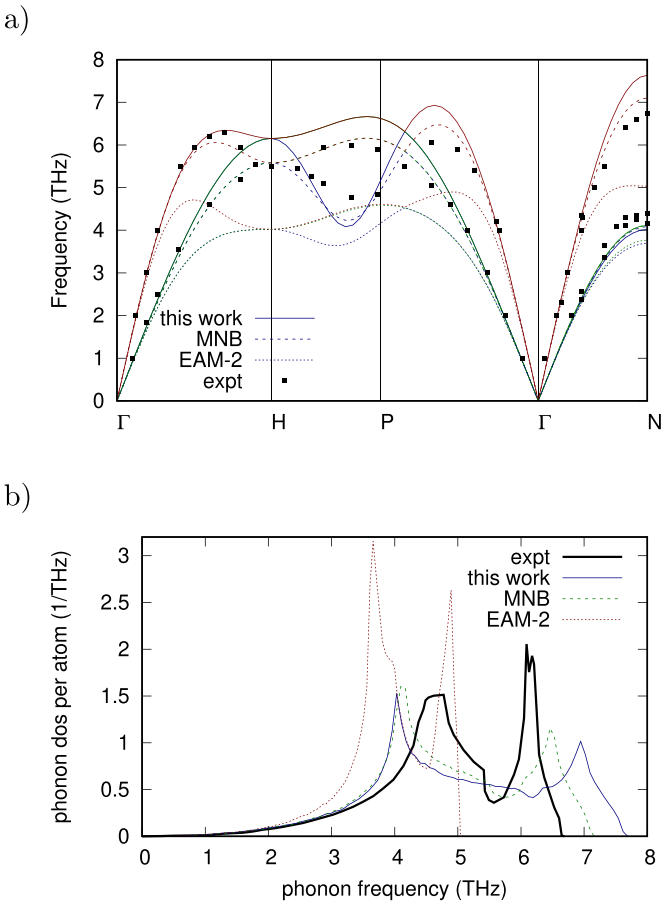

Figure 8. Computed properties of phonons in the pure tungsten crystal. Experimental points from Landolt and Börnstein [70]. (a) The phonon dispersion along high symmetry directions. (b) The phonon density of states per atom (normalised to give an area under the curve = 3.0).

Table 3. Properties of the H–H potential. A comparison is given to the empirical Wang potential [28].

Property	Units	Expt	This work	Wang
H_2 length	Å	0.74	0.744	0.726
1/2 $E_f^{H_2}$	eV	−2.26	−2.121	−2.358
H_2 spring const	eV Å^{-2}	35.95	34.44	31.0
1/3 $E_f^{H_3}$	eV		−0.808	−1.389
cohesive E hcp	eV		0.990	1.386

2.3. H–H properties

Though much is known about molecular hydrogen, classical empirical potentials can only reproduce a rather limited subset of their properties. The initial fit was chosen to be as close as possible to Wang *et al* [28], and a comparison of properties is given in table 3. There is little difference between the two EAM potentials, in particular note that the H_2 dimer is formed using either potential, and H_3 and close packed (hcp) hydrogen are strongly unfavoured. A direct comparison between the functional forms for this work and the Wang potential [28] is shown in figure 9. Note that we have only needed to use experimental properties of molecular hydrogen in this work. The only small change made here is increasing the binding energy at low electron density—this change allows slightly higher binding energy of the H atom to a surface. Note that while the embedding function technically starts with a square root form, the deviation from it is substantial. The majority of the work done fitting of the H–H potential was tuning the embedding function $F[\rho]$ in order to reproduce W–H binding energies.

2.4. W–H properties

The W–H interaction used an initial fit as close as possible to Wang *et al*. A direct comparison of the potential forms for this work and Wang is shown in figure 10. This work shows stronger binding at typical H-W separation distances, and weaker repulsion at short range.

The targetted properties are given in table 4. Some of the values have zero point energy contributions included. For this work, these have been computed by finding the phonon frequencies $\{\omega_i\}$ directly from the full dynamical matrix, and computing the sum $E_{\rm ZPE} = \sum_i {}^1/_2\hbar\omega_i$. The stable position for interstitial H is the tetrahedral site, with the octahedral site 0.36 eV higher in energy, in agreement with DFT. The migration barriers for a mobile interstitial H atom moving from one site to the next are illustrated in figure 2(b), and also are a good match to DFT. We have also targetted unrelaxed interstitial formation energies, a good test of the W–H potential at short bond length.

The present DFT calculations of relaxation volumes were performed for this work using the VASP *ab initio* simulation code, using the PAW method [78–80] with semi-core electrons included through the use of pseudo-potentials. It is important to emphasize that the inclusion of semi-core electrons in the valence states has a significant effect on the predicted formation energies of both vacancy and self-interstitial atom (SIA) defects for all the bcc transition metals [35, 81, 82]. In the present study of vacancy interaction with hydrogen atoms, the exchange-correlation effects were described using the Perdew–Burke–Ernzerhof generalised gradient approximation [83]. A kinetic energy cut-off of 500 eV was used, with a $5 \times 5 \times 5$ Monkhorst-Pack grid for electron density k-points employed in the case with super-cell ($5 \times 5 \times 5$) calculations. The set of hydrogen-vacancy defect clusters used was similar to those described in [84, 85] with larger super-cell size. The full cell relaxation method was used to evaluate the relaxation volumes. A comparison between fully relaxed calculations with those using the constant volume approximation in a combination with the corrected elastic dipole tensor calculations has been recently discussed in [38]. While the latter approximation can be extended to investigate the relaxation volume of radiation induced defects at mesoscopic scale in pure tungsten [37], it has been demonstrated clearly in the case of interaction between helium atoms and vacancy clusters that the former method is more reliable not only in reproducing experimental data of the lattice swelling but also the modulus change in a helium-implanted tungsten alloys.

Relaxation volumes of vacancy clusters and monovacancies filled with H are shown in figures 4(a) and (b)

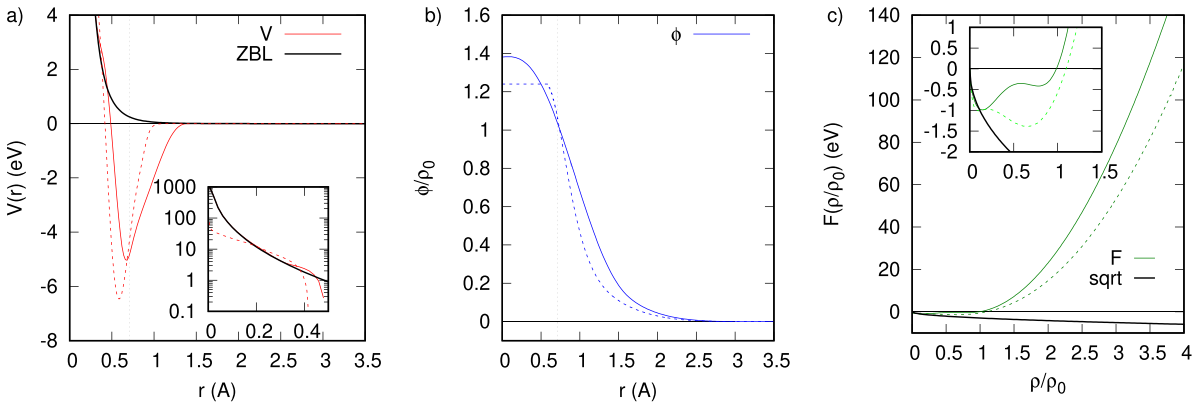

Figure 9. H–H potential comparison to [28] (dashed lines). (a) Pairwise potential, black line ZBL repulsion. (b) Density function, (c) embedding function. The vertical line in (a) and (b) indicates the dimer equilibrium spacing. The density is scaled in (b) and (c) by the level for the dimer at equilibrium spacing.

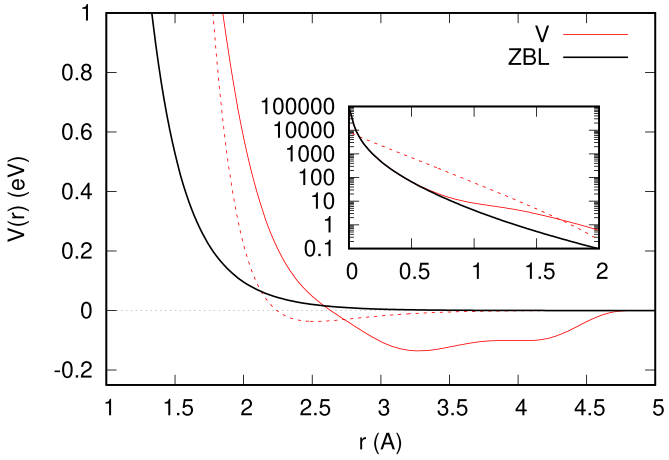

Figure 10. W–H potential comparison to [28] (dashed lines). Black line shows ZBL repulsion.

respectively. The new potential fitted here is a good match to DFT, suggesting it should well reproduce the local stresses generated by high concentrations of dissolved hydrogen gases and vacancy clusters. The relaxation volume of an H atom bound to a crowdion is found to be 1.593 Ω_0, in good agreement with the DFT value 1.719 Ω_0.

We test transferability by considering the binding of single H atoms to defect clusters, and the binding of multiple H atoms to point defects, as both these have comparable DFT calculations in the literature. Figure 11(a) shows the highest binding energy of a single H atom to interstitial clusters and $^1/_2\langle 1\,1\,1\rangle$ interstitial loops. The binding energy increases from 0.36 eV for the single SIA to 0.64 eV for a large loop ($m = 55$ interstitials, diameter 2 nm), in good accord with the DFT calculations of De Backer *et al* [10]. Figure 11(b) shows the highest binding energy of a single H atom to vacancy clusters. The binding energy increases from 1.23 eV for the monovacancy to plateau around 1.7 eV for large vacancy clusters. This increase in binding energy was reported in a DFT study by Hou *et al* [21], and is consistent with the high binding energy to a surface in the limit of infinite void size. The potential of Wang does not reproduce a significant increase in binding energy of H with the size of the vacancy cluster. Care should be taken overestimating the importance of this result in dynamic studies, as the binding energy of H to any void-space is high, so instead of finding a true thermodynamic equilibrium, MD simulations will most likely be stuck in a long-lived transient state with H atoms decorating the first vacancy cluster they encounter and rarely being detrapped.

Figure 12(a) shows the binding energy of multiple H atoms to a single interstitial, with the DFT comparison from [10]. Both the Wang potential and this work do a similarly good job reproducing the near-linear increase in total binding energy up to 12 H atoms. Figure 12(b) shows the binding energy per H atom to a single vacancy. Again, both empirical potentials are showing the correct trend, with this work producing a slightly higher binding energy, closer to DFT. The H atoms are placed at the octahedral $[^1/_2 0\,0]$ interstices.

Binding energies of an H atom to the surface are given in table 5. Note that the reference point for these energies is the vacuum level of molecular hydrogen. These energies are somewhat below that predicted by DFT and found experimentally, with the highest binding energy being 0.487 eV for an H atom on the (1 1 0) surface. Care should be therefore taken when attempting to model the equilibrium between gas phase and the surface, particularly if the [1 0 0] surface is used. Note that the Wang potential has poor surface energy properties generally, with surface energies 30% lower than DFT, and that potential only gives a positive binding energy for H on a [1 0 0] surface. The improvement made here is modest, but is the most we have been able to achieve—the near-field atomic configuration of an H atom on the surface looks similar to the atomic configuration inside a vacancy. In order to stabilise H on a surface further with an EAM potential without changing the vacancy binding energy requires a low-electron-density binding state (which can be seen in figure 9(c)), but be were not able to make this state even more binding without destabilising molecular H_2.

Table 4. Targetted properties of the W–H potential. Values in brackets include zero point energy. A comparison is given to the empirical EAM potential by Wang *et al* [28].

Category	Property	Units	DFT	Expt	This work	Wang
H in bcc W	$E_f^{H,tet}$	eV	0.93(1.04)[a], 0.685(0.95)[b]	1.04 ± 0.17	0.798(1.049)	1.056
	$E_f^{H,oct} - E_f^{H,tet}$	eV	0.44[a]		0.359	0.35
	$E_m^{H,tet-tet}$	eV	0.21[a]		0.216	0.22
	relax vol H tet	Ω_0	0.15[c]		0.133	*0.241*
	E_b^{H-H}(2nn)	eV	−0.446[d]		−0.468	−0.525
	E_b^{H-H}(3nn)	eV	−0.093[d]		−0.013	−0.112
	$E_f^{H,tet}$(unrelaxed)	eV	2.87		2.682	*0.968*
	$E_f^{H,oct}$(unrelaxed)	eV	2.81		2.629	3.217
H in vac	E_b^{v-H}	eV	1.28(1.43)[e]		1.233(1.290)	1.011
	E_b^{vH-H}	eV	1.25(1.41)[e]		1.349(1.456)	1.098
	$E_b^{vH_2-H}$	eV	1.11(1.22)[e]		0.975(1.032)	0.819
	$E_b^{vH_3-H}$	eV	1.00(1.11)[e]		1.050(1.074)	0.688
	$E_b^{vH_4-H}$	eV	0.91(1.00)[e]		0.705(0.742)	0.561
	$E_b^{vH_5-H}$	eV	0.32(0.47)[e]		0.486(0.670)	0.285
	$E_b^{H\text{sub}}$	eV			0.375	0.550
	Ω_{rel}^{vH}	Ω_0	−0.24		−0.273	*−0.027*
	$\Omega_{\text{rel}}^{vH_2}$	Ω_0	−0.205		−0.232	*0.008*
	$\Omega_{\text{rel}}^{vH_3}$	Ω_0	−0.170		−0.256	*0.119*
	$\Omega_{\text{rel}}^{vH_4}$	Ω_0	−0.131		−0.216	*0.263*
	$\Omega_{\text{rel}}^{vH_5}$	Ω_0	−0.094		−0.121	*0.429*
	$\Omega_{\text{rel}}^{vH_6}$	Ω_0	−0.055		−0.043	*0.774*
H + int	E_b^{i-H}	eV	0.33[c]		0.357	0.416
H + surface	E_b[100]	eV	0.93[f]	0.7,0.82[f]	*0.312(0.466)*	*0.146*

[a] Fernandez *et al* [73].
[b] Heinola and Ahlgren[74].
[c] De Backer *et al* [10].
[d] Liu *et al* [75].
[e] Heinola *et al* [76].
[f] Johnson and Carter[77].
The binding energy for a pair of H interstitial atoms is given for tetrahedral sites separated by $[\frac{1}{2}\,0\,0]$ and $[\frac{1}{2}\,\frac{1}{4}\,\frac{1}{4}]$.
In this table and subsequently, italics indicate values which could produce significant errors in simulation. These values are discussed in the text.

3. Large defect clusters in a hydrogen-rich atmosphere

In this section we consider how the energy levels of prototypical nanoscale lattice defects produced by radiation damage [86] are affected by the binding of multiple hydrogen isotope atoms. There is little DFT data for larger clusters, so the results in this section are predictions made with the current empirical potential, together with a discussion of where they may prove important for gas retention studies.

In this section, the 'best' relaxed structures were found by a random sampling process. First, the extended defect in pure W was constructed and relaxed at constant volume using conjugate gradients. The supercell size was $32 \times 32 \times 32$ conventional unit cells, and the defect was taken to be either a circular loop or spherical void containing about 60 point defects. Any empty space regions were then detected with the void isosurface detection method of [40]. H atoms were then placed into these void regions, with an artificial repulsion keeping the unrelaxed H positions $>3\times$ the H_2 dimer length apart. Any surplus H atoms were added to tetrahedral lattice sites at random. The decorated defect was then relaxed again using conjugate gradients. We considered 1000 initial configurations at order 1 H per point defect, rising to 10 000 initial configurations at 5 H per point defect. We cannot say that the structures produced are guaranteed to be the lowest possible energy structures, only that they represent carefully chosen low energy structures. At finite temperature, the configurational entropy associated with a large number of similar-energy configurations will become more important than the true 0 K minimum. Subsequent thermal annealing with 1 ns MD at up to 900 K does not show any significant structural transformation in these defects, indicating they are reasonably stable.

In figure 13(a) we plot the binding energy of multiple H atoms to interstitial dislocation loops, in terms of binding energy of H atoms to an existing loop, ie the quantity $E_b(I_mH_n) = E_f(I_mH_0) + nE_f(H) - E_f(I_mH_n)$, where $E_f(I_mH_n)$ is the formation energy of the m interstitial loop decorated with n H atoms. In this figure we have created circular dislocation loops with radius $3a_0$, giving a diameter of about 2 nm—around 60 interstitials. In both the $\langle 1\,0\,0\rangle$ and $\frac{1}{2}\langle 1\,1\,1\rangle$ Burgers vector cases, the H atoms are bound close to the dislocation core. At higher ratios of H atoms to interstitials, excess H atoms are weakly bound in the region of tensile stress just outside the disc of inserted atoms. The binding energy per H atom is greater to the [1 0 0] loop than to the $\frac{1}{2}$[1 1 1] loop, as the

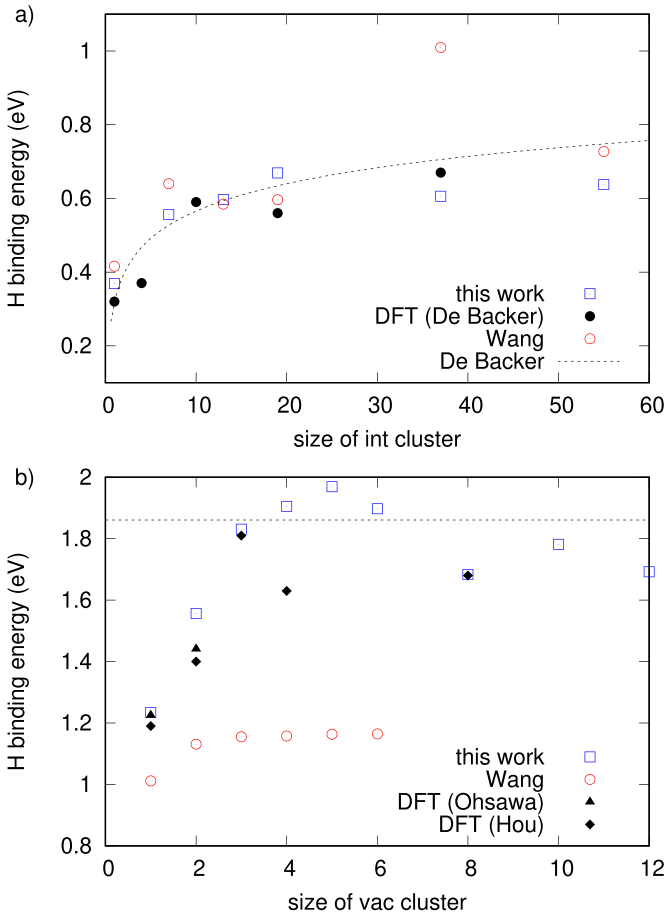

Figure 11. Binding energy of single hydrogen atoms to extended defects in tungsten. (a) Binding energy to interstitial clusters and $^1/_2\langle 1\,1\,1\rangle$ loops. The dashed line indicates the fit suggested in [10]. (b) Binding energy to vacancy clusters. The dashed line indicates the binding energy of the [0 0 1] surface from [84]. DFT values from De Backer *et al* [10], Hou *et al* [21], and Ohsawa and Kuramoto [85].

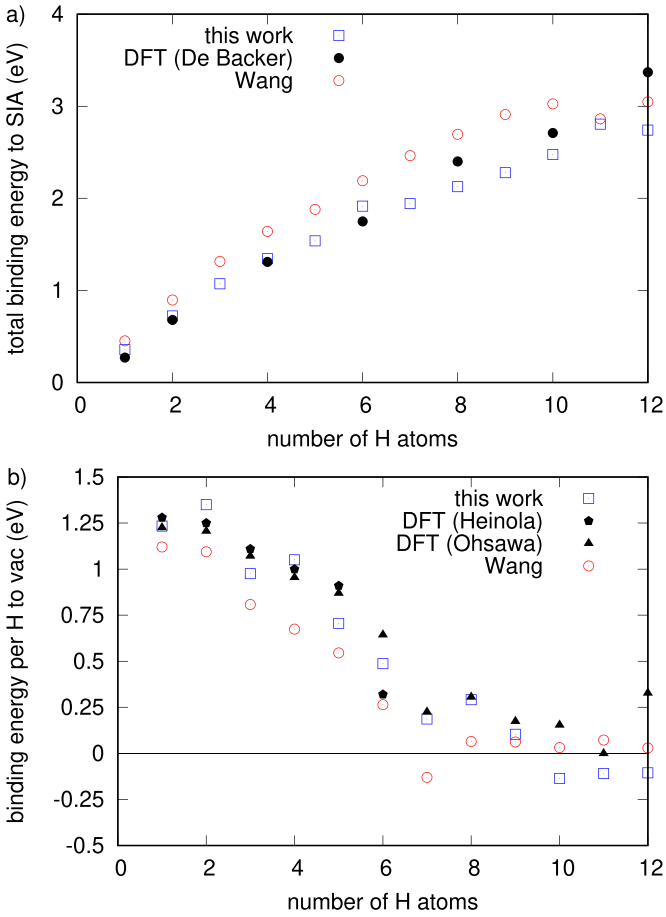

Figure 12. Binding energy of multiple hydrogen atoms to point defects in tungsten. (a) Total binding energy to single SIA (crowdion). (b) Total binding energy to monovacancy. DFT values from De Backer *et al* [10], Heinola and Ahlgren [84], and Ohsawa and Kuramoto [85].

former has the larger Burgers vector and so creates a greater tensile stress. Figure 13(b) replots the data as the total binding energy bringing all interstitials and H atoms from infinity, ie the quantity $E_b^{\rm tot}(I_mH_n) = (N+m)E_0 + mE_f(I_1H_0) + nE_f(H) - E_f(I_mH_n)$, where the simulation cell has N bcc lattice sites. Though the undecorated $^1/_2\langle 1\,1\,1\rangle$ loop has higher binding energy than the $\langle 1\,0\,0\rangle$ loop, adding H atoms brings the total formation energy of the $\langle 1\,0\,0\rangle$ loop down faster, giving a crossover point between them at $m/n \sim 0.25$. As noted above, in this empirical potential, the energy gap between $\langle 1\,0\,0\rangle$ and $^1/_2\langle 1\,1\,1\rangle$ is smaller than that predicted by DFT, so we should expect this crossover point to be higher in reality. The qualitative result that dissolved hydrogen isotope gas should stabilise $\langle 1\,0\,0\rangle$ loops is likely to be robust.

Figure 13(c) shows the relaxation volume per H atom, computed from the dipole tensor and the elastic constants [87]. We see that each H atom contributes a small positive volume change, smaller than that of the interstitial H in a tetrahedral position in the perfect lattice. This volume change is in addition to the much greater relaxation volume of the interstitial loop itself, order $m\Omega_0$, indicating that an H atom brought from infinity to the loop will reduce the total elastic stress, but only slightly. There is little difference between loops with $\langle 1\,0\,0\rangle$ and $^1/_2\langle 1\,1\,1\rangle$ Burgers vectors. This result suggests little is to be gained in terms of reducing elastic stress build up by binding H atoms to interstitial defects, and coupled with the low binding energy per gas atom seen in figure 13(a), we conclude that using this potential at room temperature and above there will be little hydrogen gas associated with interstitial loops except under plasma loading conditions. This is in line with the conclusions of the meso-scale study in [10].

Figure 14(a) shows the binding energy of H atoms to vacancy-type defects, $E_b(V_mH_n) = E_f(V_mH_0) + nE_f(H) -$

Table 5. Surface binding energies of H on W, computed as $E_f(\text{surface}) + 1/2\text{E}_\text{f}(\text{H}_2) - \text{E}_\text{f}(\text{surface : H})$. DFT and experimental values reported in [77]. Figures in brackets include zero point energy contributions.

Property	DFT	Expt	This work	Wang
[1 1 0]	0.75		0.487(0.722)	−0.291
[2 1 1]			0.389(0.707)	−0.024
[1 1 1]			0.394(0.696)	0.001
[1 0 0]	0.93	0.7, 0.82	0.312(0.466)	0.146

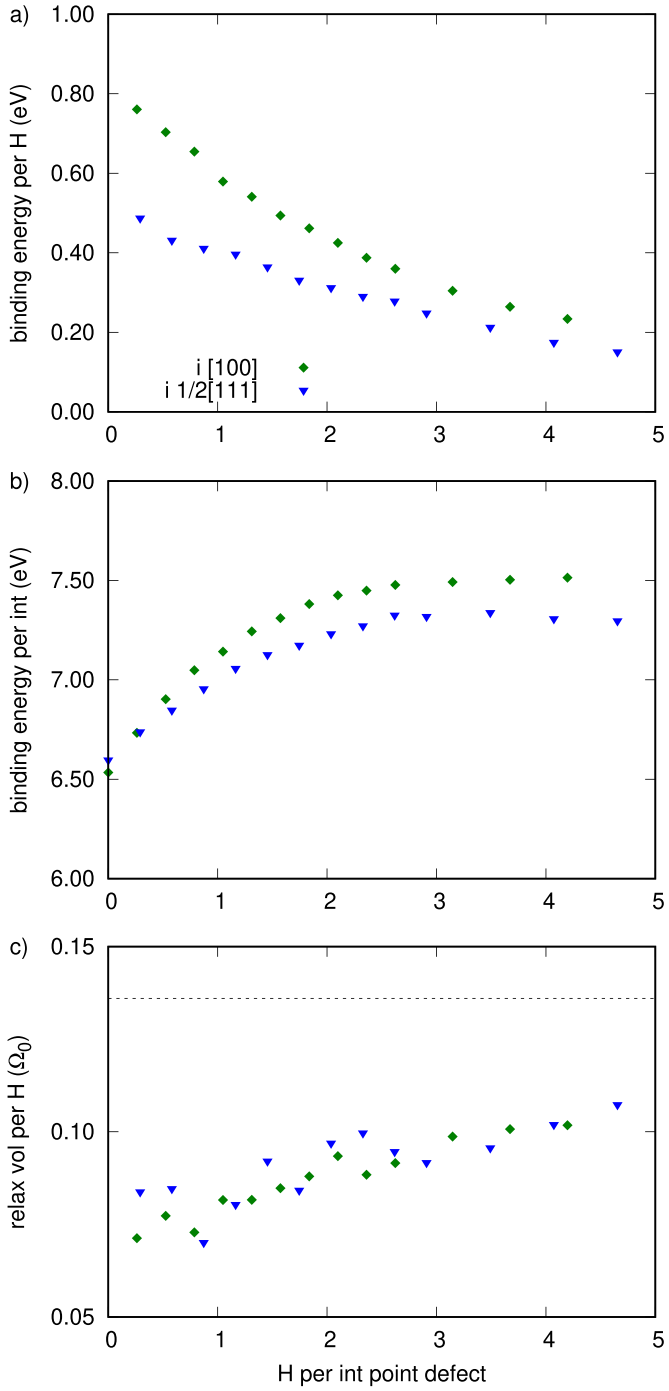

Figure 13. Interaction of hydrogen atoms with extended interstitial-type defects in tungsten as a function of the ratio of H atoms to point defects. (a) Binding energy per H atom to interstitial clusters and dislocation loops. (b) Total binding energy per interstitial (binding energy of interstitial defect and binding energy of H atoms) for extended interstitial defects. (c) Relaxation volume per bound H atom, expressed as a fraction of the volume per tungsten atom Ω_0. Dashed line shows relaxation volume of a single H atom in the tetrahedral position in perfect W.

$E_f(V_mH_n)$. Here we have considered the circular dislocation loops with Burgers vectors $\langle 1\,0\,0\rangle$ and $^1/_2\langle 1\,1\,1\rangle$, as well as the spherical void and the 'open' vacancy loop [31]—a platelet of vacancies with habit plane $\langle 1\,0\,0\rangle$ and $^1/_2\langle 1\,1\,1\rangle$ formed when the atomic planes inside the corresponding prismatic dislocation loop are separated. All defects have around 60 unoccupied lattice sites. As with the binding to interstitial loops, we see H atoms trapped near the vacancy loop dislocation cores, and with higher binding energies than the interstitial counterparts. This binding energy is slowly reduced as the ratio of H to vacancies is increased. The open defects, the void and the vacancy platelets, have higher binding energy than the dislocation loops. It is notable that some vacancy platelets have higher binding even than the void, which is likely due to a single H atom being able to stabilise the electron-deficient W atoms on either side of the platelet.

In figure 14(b) we replot the data using the total binding energy of the defect plus the binding of the H atoms per vacant lattice site, $E_b^{\rm tot}(V_mH_n) = (N-m)E_0 + mE_f(V_1H_0) + nE_f(H) - E_f(V_mH_n)$. Here we see that the void is by far the strongest bound defect per vacancy at this defect size, which is to be expected as the energy of the open defects scales with surface area. At high H occupation, $n/m > 1$, it appears the binding energy per vacancy is greater than the formation energy per vacancy. This does not mean that a void can spontaneously form—that would require the emission of interstitials which are very high energy point defects. At low H occupation, $n/m \ll 1$, we see the vacancy dislocation loops are the second most stable defects, with the platelets very similar at this defect size. But as with the interstitial loop case, increasing the number of H atoms changes this order, and the $\langle 1\,0\,0\rangle$ platelet is more stable with only a few added H atoms present. At higher ratios $n/m > 0.6$, the $^1/_2\langle 1\,1\,1\rangle$ platelet becomes more stable than the dislocation loop, and at $n/m > 3$, the platelets have similar stability to the void. These observations from the empirical potential, suggest that in a rich hydrogen isotope atmosphere condition, such as might be found in a plasma loading condition, there is a driving force for transformation between dislocation loops and open platelets.

The relaxation volume per H atom bound to vacancy defects is shown in figure 14(c). In contrast to the result for interstitial loops, here we see considerably more structure. H atoms bound to dislocation loops show a greater relaxation volume than in the tetrahedral interstitial position, which acts to alleviate the large negative relaxation volume (order $-m\Omega_0$) of the vacancy loop itself. For open-volume defects—the void and plates considered here—the relaxation volume is very small for the first few gas atoms binding to the surface of the defect, as these do not contribute significant additional surface stress. Figure 14(d) shows the total relaxation volume per vacancy for H decorated vacancy defects. As the H level increases, so does the relaxation volume. Of particular note is that at around 2 H per vacancy, the *sign* of the relaxation volume of the open defects changes from negative to positive. This result shows that non-zero stress applied as boundary conditions, or as locally varying stresses due to nearby defects, will further change the energy levels of the defects. In particular this result suggests that under tensile stress conditions, produced by interstitial defects in the early stages of radiation damage [13], open structures may be further favoured. Further study of this effect is beyond the scope of this paper, but warrants future investigation.

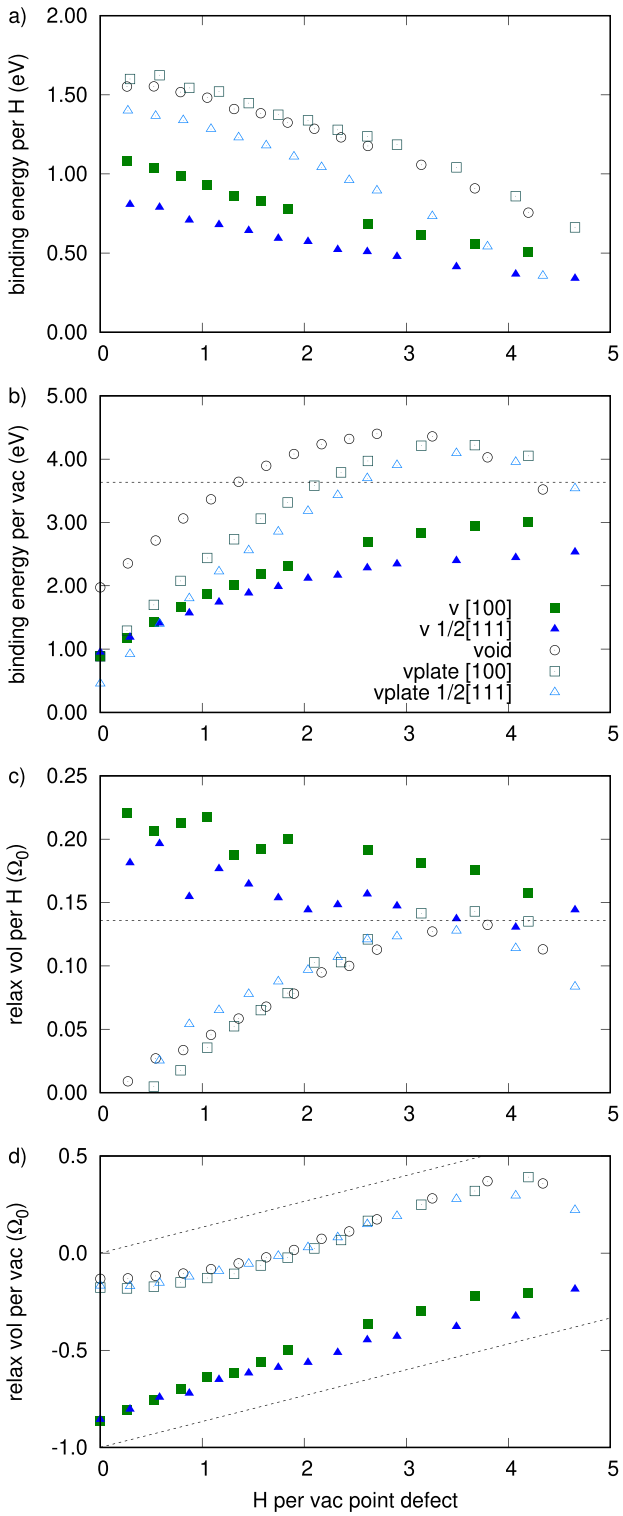

Figure 14. Interaction of hydrogen atoms with extended vacancy-type defects in tungsten as a function of the ratio of H atoms to point defects. (a) Binding energy per H atom to extended vacancy defects. (b) Total binding energy per vacancy (binding energy of vacancy defect and binding energy of H atoms) for extended vacancy defects. Dashed line is the monovacancy formation energy for comparison. (c) Relaxation volume per bound H atom, expressed as a fraction of the volume per tungsten atom Ω_0. Dashed line shows relaxation volume of a single H atom in the tetrahedral position in perfect W. (d) Total relaxation volume per vacancy. Dashed lines show the gradient of the corresponding relaxation volume of H atoms in perfect W.

Figure 15 shows renderings of some of the decorated defects. We have used the method of [40] to find void isosurfaces, and DXA [88, 89] to find dislocation lines. Two sets of images are shown, with filling ratios $n/m \sim 1$ and $n/m \sim 4$. At $n/m \sim 1$, the dislocation loop defects are easily identifiable as such, with a small number of H atoms decorating the

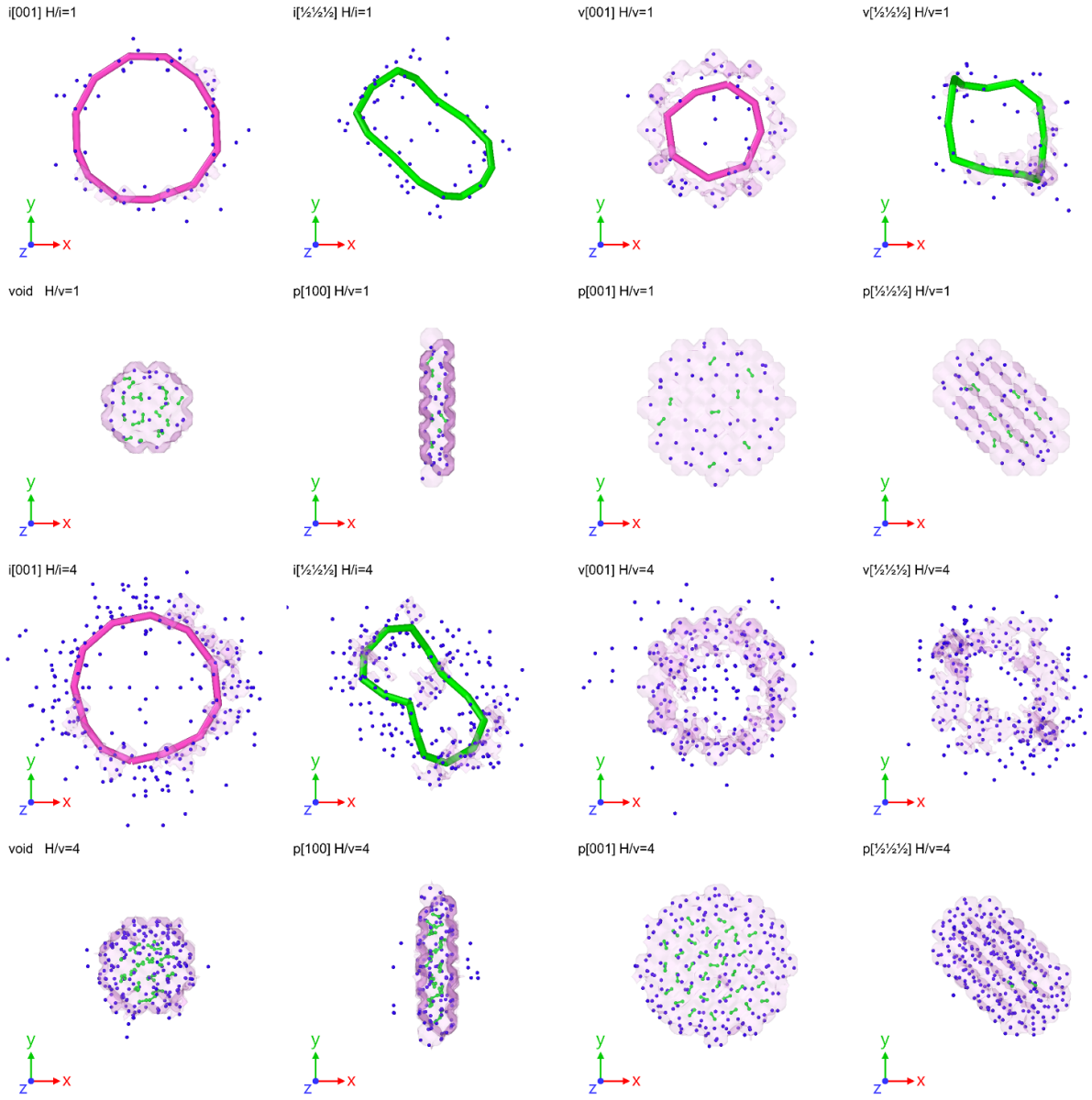

Figure 15. Extended defects in tungsten decorated with multiple H atoms. Each has a size of around 60 point defects, making the loops and plates ∼2 nm diameter, and the void ∼1.5 nm diameter. The top row, left-to-right, shows interstitial loops with $\langle 1\,0\,0\rangle$ and $^1/_2\langle 1\,1\,1\rangle$ Burgers vectors, decorated with 64 H ($n/m \sim 1$), then vacancy loops with $\langle 1\,0\,0\rangle$ and $^1/_2\langle 1\,1\,1\rangle$ Burgers vectors. H atoms are shown as blue dots. The second row shows a void, then a open vacancy platelet in $[1\,0\,0]$, $[0\,0\,1]$, and $^1/_2\langle 1\,1\,1\rangle$ orientation. H_2 molecules are indicated as green dumbbells. The third and fourth rows show the same defects decorated with 256 H ($n/m \sim 4$). Pink lines show $\langle 1\,0\,0\rangle$ edge dislocation lines, green lines show $\langle 1\,1\,1\rangle$ edge dislocation lines. Purple surfaces show boundaries of cavity regions. Tungsten atoms not shown. Rendered with OVITO [88].

dislocation lines. Void spaces do arise between W atoms even at low n/m, but they appear as cracks, significantly thinner than a monovacancy, between W atoms under considerable tensile strain in the direction of the Burgers vector. In the open defects (voids and platelets) molecular H_2 can be seen in the interior, with H atoms also decorating the surface. At $n/m \sim 4$, the interstitial dislocation loops are still identifiable, but the vacancy dislocation loops have lost their cores, instead appearing closer to a thin toroidal crack between the atoms in the direction of the Burgers vector. No molecular H_2 is observed in decorated vacancy loops. No spontaneous interstitial ejection is observed in any structure.

It is notable that some H sits in interstitial positions beyond the defect. This observation of a Cottrell atmosphere of H atoms in the elastic field of an extended defect was seen previously by De Backer *et al* [10] using a core–shell model for the binding energy and Metropolis Monte Carlo to generate low energy decorated structures.

4. Conclusions

No empirical potential is expected to perfectly reproduce all properties, especially those outside the targetted set, and this potential is no exception. We have tried to report faithfully areas where there could be concerns. We therefore note

- The trivacancy migration energy in pure W is close to the monovacancy migration energy, and is not the very low value found by DFT. This is a failure of the EAM potential form to reproduce the correct sp-d hybridization and can not be easily fixed. This may have an impact in studies concerning the clustering of monovacancies.
- The (1 0 0) surface energy of pure W is ordered incorrectly, again as a failure of the EAM potential form to reproduce the correct sp-d hybridization. The (1 0 0) surface should be treated as least reliable in quantitative studies.
- The binding energy of an H atom to a surface is low, ranging from 0.3 to 0.5 eV compared to the experimental value 0.7–0.8 eV. While this is an improvement on previous literature potentials, it is most likely related again to the difficulty of reproducing surface electron states. This may have an impact where equilibrium between molecular H_2 and the surface is required.

We have shown that the potential described here is capable of reproducing a range of DFT-calculated properties of the interactions between hydrogen isotope gases dissolved in a tungsten lattice, and point- and extended-lattice defects introduced by irradiation damage. In particular, we have focused on ensuring that not only the binding energies, but also the relaxation volumes of the defects are well reproduced. This gives us more confidence that the potential will show qualitatively correct trends as a function of the applied boundary conditions of stress and strain.

Data availability statement

All data that support the findings of this study are included within the article (and any supplementary files).

Acknowledgments

We are grateful to K Heinola and C Becquart for helpful discussions, and L Yang for providing the LAMMPS potential files for their tungsten-hydrogen potential. This work has been carried out within the framework of the EUROfusion Consortium, funded by the European Union via the Euratom Research and Training Programme (Grant Agreement No. 101052200—EUROfusion), and by the RCUK Energy Programme, Grant No. EP/W006839/1. To obtain further information on the data and models underlying the paper please contact PublicationsManager@ukaea.uk. The views and opinions expressed herein do not necessarily reflect those of the European Commission. Computer time granted by the IT Center for Science – CSC – Finland is gratefully acknowledged.

Author contributions

D R M developed the concept, fitted the potential, and generated results using the potential. D N-M performed the DFT calculations and contributed to the development of the model. V W L and F G G performed MD testing under a range of conditions, M Yu L generated results using empirical potentials and contributed to the development of the model.

Appendix. Parameterization

In this section we present the parameterization of the potential.

The explicit form chosen for the three functions is

$$V(r) = \begin{cases} Z(r) + P_V^{(0)}(r) & , \quad 0 \leqslant r \leqslant r_V^{(1)} \\ Z(r) + P_V^{(1)}(r) & \quad r_V^{(1)} \leqslant r \leqslant r_V^{(2)} \\ P_V^{(2)}(r) & \quad r_V^{(2)} \leqslant r \leqslant r_V^{(3)} \\ 0 & \quad r \geqslant r_V^{(3)} \end{cases}$$

$$\phi(x) = \begin{cases} P_\phi^{(0)}(r) & , \quad 0 \leqslant r \leqslant r_\phi^{(1)} \\ P_\phi^{(1)}(r) & \quad r_\phi^{(1)} \leqslant r \leqslant r_\phi^{(2)} \\ 0 & \quad r \geqslant r_\phi^{(2)} \end{cases}$$

$$F(\rho) = \begin{cases} \alpha\sqrt{\rho} + P_F^{(0)}(\rho) & , \quad 0 \leqslant \rho \leqslant \rho^{(1)} \\ \alpha\sqrt{\rho} + P_F^{(1)}(\rho) & \quad \rho^{(1)} \leqslant \rho \leqslant \rho^{(2)} \\ \alpha\sqrt{\rho} & \quad \rho \geqslant \rho_\phi^{(2)} \end{cases} , \quad (3)$$

where the functions $P_\sigma^{(n)}(x)$ are fifth-order polynomials which match zeroth, first, and second derivatives at the knot points $x_\sigma^{(n)}$. The full parameterization is given in table 6. We also constrain by *fiat* some of the values and derivatives at zero or the cutoff range, to ensure continuity and smoothness.

The functional form of $P_\sigma^{(n)}(x)$ can be found by substituting into the general polynomial form

$$\begin{aligned} P_\sigma^{(n)}(z) &= P_0 + P_0' z + P_0'' z^2/2 \\ &= -(20P_0 - 20P_1 + 12P_0' + 8P_1' + 3P_0'' - P_1'')z^3/2 \\ &\quad + (30P_0 - 30P_1 + 16P_0' + 14P_1' + 3P_0'' - 2P_1'')z^4/2 \\ &\quad - (12P_0 - 12P_1 + 6P_0' + 6P_1' + P_0'' - P_1'')z^5/2, \end{aligned} \quad (4)$$

where $z = (x_\sigma^{(n)} - x)/(x_\sigma^{(n)} - x_\sigma^{(n-1)})$, and $P_{0,1}, P_{0,1}', P_{0,1}''$ are the values of the function and its derivatives with respect to z which are matched at either end of the interval. Note that in table 6 we present the derivatives with respect to x not z.

To the repulsive pairwise potential we add the ZBL form between $r = 0$ and $r = r_2$. This has the universal form reproduced here for completeness

$$\begin{aligned} V_{\mathrm{ZBL}}(r) = \frac{Z_1 Z_2}{4\pi\varepsilon r} \big(& 0.1818\,\mathrm{e}^{-3.2x/a} + 0.5099\,\mathrm{e}^{-0.9423x/a} \\ & + 0.2802\,\mathrm{e}^{-0.4029x/a} + 0.02817\,\mathrm{e}^{-0.2016x/a} \big), \end{aligned} \quad (5)$$

Table 6. Full parameterization of the potential, defined as function values and derivatives at knot points. Lengths (x) in Å, energies (V, F) in eV.

$F_{\mathrm{W}}(\rho)$							
α	−10.392 487 15						
ρ_0	0	$F(\rho_0)$	0	$F'(\rho_0)$	2.069 577 25	$F''(\rho_0)$	−5.116 781 24
ρ_1	0.660 597 43	$F(\rho_1)$	0.619 680 10	$F'(\rho_1)$	−1.079 627 70	$F''(\rho_1)$	0.958 866 30
ρ_2	1.052 264 57	$F(\rho_2)$	0	$F'(\rho_2)$	0	$F''(\rho_2)$	0
$\phi_{\mathrm{W}}(r)$							
r_0	0	$\phi(r_0)$	0.513 046 56	$\phi'(r_0)$	−0.266 141 97	$\phi''(r_0)$	0.062 741 33
r_1	3.273 329 80	$\phi(r_1)$	0.045 215 07	$\phi'(r_1)$	−0.074 992 84	$\phi''(r_1)$	0.064 327 26
r_2	4.649 955 91	$\phi(r_2)$	0	$\phi'(r_2)$	0	$\phi''(r_2)$	0
$F_{\mathrm{H}}(\rho)$							
α	−2.094 997 341						
ρ_0	0	$F(\rho_0)$	0	$F'(\rho_0)$	−0.999 828 063	$F''(\rho_0)$	13.297 127 96
ρ_1	2.206 458 605	$F(\rho_1)$	3.026 5026	$F'(\rho_1)$	2.597 429 616	$F''(\rho_1)$	6.826 075 643
ρ_2	232.470 2459	$F(\rho_2)$	0	$F'(\rho_2)$	0	$F''(\rho_2)$	0
$\phi_{\mathrm{H}}(r)$							
r_0	0	$\phi(r_0)$	3.150 746 82	$\phi'(r_0)$	0.081 501 79	$\phi''(r_0)$	0.023 703 87
r_1	1.739 569 71	$\phi(r_1)$	0.21 459 106	$\phi'(r_1)$	−0.585 589 91	$\phi''(r_1)$	1.401 275 98
r_2	3.059 538 85	$\phi(r_2)$	0	$\phi'(r_2)$	0	$\phi''(r_2)$	0
$V_{\mathrm{WW}}(r)$							
r_0	0	$V(r_0)$	0	$V'(r_0)$	0	$V''(r_0)$	0
r_1	2.756 823 38	$V(r_1)$	−0.360 458 09	$V'(r_1)$	0.788 131 64	$V''(r_1)$	−1.388 444 45
r_2	3.095 505 08	$V(r_2)$	−0.161 344 21	$V'(r_2)$	0.232 114 07	$V''(r_2)$	3.092 847 96
r_3	4.447 465 15	$V(r_3)$	0	$V'(r_3)$	0	$V''(r_3)$	0
$V_{\mathrm{WH}}(r)$							
r_0	0	$V(r_0)$	0	$V'(r_0)$	0	$V''(r_0)$	0
r_1	1.483 013 29	$V(r_1)$	2.421 633 09	$V'(r_1)$	−7.641 619 63	$V''(r_1)$	10.586 129 68
r_2	2.671 176 36	$V(r_2)$	−0.126 279 64	$V'(r_2)$	−0.414 496 13	$V''(r_2)$	0.249 454 55
r_3	3.967 808 40	$V(r_3)$	0	$V'(r_3)$	0	$V''(r_3)$	0
r_4	4.844 774 78	ΔV	−0.100 567 16				
$V_{\mathrm{HH}}(r)$							
r_0	0	$V(r_0)$	0	$V'(r_0)$	0	$V''(r_0)$	0
r_1	0.299 325 96	$V(r_1)$	−0.002 775 62	$V'(r_1)$	−0.011 039 95	$V''(r_1)$	504.901 7561
r_2	0.739 727 33	$V(r_2)$	−4.653 878 43	$V'(r_2)$	14.211 494 52	$V''(r_2)$	−74.740 558 20
r_3	1.412 690 52	$V(r_3)$	0	$V'(r_3)$	0	$V''(r_3)$	0

with $Z_{1(2)}$ being the atomic number of element 1(2), and $a =$ 0.078 908 Å the screening length constant.

Finally, in order to increase the binding of hydrogen atoms to surfaces, we further add a long range attractive interaction to the V_{WH} potential, of the form $V^{+}(r) = V_0$, $r < r_3$, tapering to zero at $r = r_4$.

ORCID iDs

Daniel R Mason https://orcid.org/0000-0002-1536-6254
Duc Nguyen-Manh https://orcid.org/0000-0001-6061-9946
Victor W Lindblad https://orcid.org/0009-0004-3416-2750
Fredric G Granberg https://orcid.org/0000-0001-9058-5652
Mikhail Yu Lavrentiev https://orcid.org/0000-0001-9899-1700

References

[1] You J H *et al* 2016 *Nucl. Mater. Energy* **9** 171
[2] Gilbert M R, Zheng S, Kemp R, Packer L W, Dudarev S L and Sublet J-C 2014 *Fusion Sci. Technol.* **66** 9
[3] Keys L K, Smith J P and Moteff J 1968 *Phys. Rev.* **176** 851
[4] Hirai T *et al* 2016 *Nucl. Mater. Energy* **9** 616
[5] Li M and You J-H 2018 *Nucl. Mater. Energy* **14** 1

[6] You J *et al* 2021 *J. Nucl. Mater.* **544** 152670
[7] Ogorodnikova O and Gann V 2015 *J. Nucl. Mater.* **460** 60
[8] Ogorodnikova O V 2015 *J. Appl. Phys* **118** 074902
[9] De Backer A, Mason D R, Domain C, Nguyen-Manh D, Marinica M-C, Ventelon L, Becquart C S and Dudarev S L 2017 *Phys. Scr.* **T170** 014073
[10] De Backer A, Mason D R, Domain C, Nguyen-Manh D, Marinica M-C, Ventelon L, Becquart C S and Dudarev S L 2018 *Nucl. Fusion* **58** 016006
[11] Wang J *et al* 2021 *J. Nucl. Mater.* **545** 152749
[12] Hollingsworth A *et al* 2019 *Nucl. Fusion* **60** 016024
[13] Mason D R *et al* 2020 *Phys. Rev. Lett.* **125** 225503
[14] Wang J, Chai J, Dang W, Pan X-D, Li X-C and Luo G-N 2022 *Nucl. Mater. Energy* **33** 101260
[15] Kato D, Iwakiri H, Watanabe Y, Morishita K and Muroga T 2015 *Nucl. Fusion* **55** 083019
[16] Schwarz-Selinger T, Bauer J, Elgeti S and Markelj S 2018 *Nucl. Mater. Energy* **17** 228
[17] Liu Y-N, Ahlgren T, Bukonte L, Nordlund K, Shu X, Yu Y, Li X-C and Lu G-H 2013 *AIP Adv.* **3** 122111
[18] Qin S-Y, Jin S, Sun L, Zhou H-B, Zhang Y and Lu G-H 2015 *J. Nucl. Mater.* **465** 135
[19] Zayachuk Y, 't Hoen M, van Emmichoven P Z, Terentyev D, Uytdenhouwen I and van Oost G 2013 *Nucl. Fusion* **53** 013013
[20] Hodille E A, Fernandez N, Piazza Z A, Ajmalghan M and Ferro Y 2018 *Phys. Rev. Mater.* **2** 093802
[21] Hou J, Kong X-S, Wu X, Song J and Liu C 2019 *Nat. Mater.* **18** 833
[22] Derlet P M and Dudarev S L 2020 *Phys. Rev. Mater.* **4** 023605
[23] Granberg F, Byggmästar J and Nordlund K 2021 *J. Nucl. Mater.* **556** 153158
[24] Li X-C, Shu X, Liu Y-N, Gao F and Lu G-H 2011 *J. Nucl. Mater.* **408** 12
[25] Juslin N and Wirth B 2013 *J. Nucl. Mater.* **432** 61
[26] Hodille E A, Ferro Y, Fernandez N, Becquart C S, Angot T, Layet J M, Bisson R and Grisolia C 2016 *Phys. Scr.* **T167** 014011
[27] Bonny G, Grigorev P and Terentyev D 2014 *J. Phys.: Condens. Matter* **26** 485001
[28] Wang L-F, Shu X, Lu G-H and Gao F 2017 *J. Phys.: Condens. Matter* **29** 435401
[29] Marenkov E, Tsvetkov I, Pisarev A, Gasparyan Y M and Rusinov A 2011 *Nucl. Instrum. Methods Phys. Res.* B **269** 876
[30] Zibrov M and Schmid K 2022 *Nucl. Mater. Energy* **30** 101121
[31] Gilbert M R, Dudarev S L, Derlet P M and Pettifor D G 2008 *J. Phys.: Condens. Matter* **20** 345214
[32] Fikar J, Schäublin R, Mason D R and Nguyen-Manh D 2018 *Nucl. Mater. Energy* **16** 60
[33] Hou J, Kong X-S, Sun J, You Y-W, Wu X, Liu C S and Song J 2018 *Nucl. Fusion* **58** 096021
[34] Nguyen-Manh D and Dudarev S L 2015 *Nucl. Instrum. Methods Phys. Res.* B **352** 86
[35] Hofmann F, Nguyen-Manh D, Gilbert M, Beck C, Eliason J K, Maznev A, Liu W, Armstrong D E J, Nelson K A and Dudarev S L 2015 *Acta Mater.* **89** 352
[36] Mason D R, Nguyen-Manh D and Becquart C S 2017 *J. Phys.: Condens. Matter* **29** 505501
[37] Mason D, Nguyen-Manh D, Marinica M-C, Alexander R and Dudarev S 2019 in preparation
[38] Wrobel J S, Zembla M R, Nguyen-Manh D, Olsson P, Messina L, Domain C, Wejrzanowski T and Dudarev S L 2021 *Comput. Mater. Sci.* **194** 110435
[39] Muzyk M, Nguyen-Manh D, Kurzydłowski K J, Baluc N L and Dudarev S L 2011 *Phys. Rev.* B **84** 104115
[40] Mason D R, Granberg F, Boleininger M, Schwarz-Selinger T, Nordlund K and Dudarev S L 2021 *Phys. Rev. Mater.* **5** 095403
[41] Simmonds M, Wang Y, Barton J, Baldwin M, Yu J, Doerner R and Tynan G 2017 *J. Nucl. Mater.* **494** 67
[42] Simmonds M, Schwarz-Selinger T, Patino M, Baldwin M, Doerner R and Tynan G 2022 *Nucl. Fusion* **62** 036012
[43] Daw M S and Baskes M I 1984 *Phys. Rev.* B **29** 6443
[44] Plimpton S 1995 *J. Comput. Phys.* **117** 1
[45] Finnis M W and Sinclair J E 1984 *Phil. Mag.* A **50** 45
[46] Ackland G and Thetford R 1987 *Phil. Mag.* A **56** 15
[47] Björkas C, Nordlund K and Dudarev S L 2009 *Nucl. Instrum. Methods Phys. Res.* B **267** 3204
[48] Becquart C S, De Backer A, Olsson P and Domain C 2021 *J. Nucl. Mater.* **547** 152816
[49] Ziegler J, Biersack J and Littmark U 1982 *The Stopping and Range of Ions in Solids* (Pergamon)
[50] Ackland G J, Finnis M W and Vitek V 1988 *J. Phys. F: Met. Phys.* **18** L153
[51] Marinica M-C, Ventelon L, Gilbert M R, Proville L, Dudarev S L, Marian J, Bencteux G and Willaime F 2013 *J. Phys.: Condens. Matter* **25** 395502
[52] Heinola K, Djurabekova F and Ahlgren T 2017 *Nucl. Fusion* **58** 026004
[53] Kong X-S, Wang S, Wu X, You Y-W, Liu C, Fang Q, Chen J-L and Luo G-N 2015 *Acta Mater.* **84** 426
[54] Mason D R, Nguyen-Manh D, Marinica M-C, Alexander R, Sand A E and Dudarev S L 2019 *J. Appl. Phys.* **126** 075112
[55] Featherston F H and Neighbours J R 1963 *Phys. Rev.* **130** 1324
[56] Varvenne C, Bruneval F, Marinica M-C and Clouet E 2013 *Phys. Rev.* B **88** 134102
[57] Ma P-W, Mason D R and Dudarev S L 2020 *Phys. Rev. Mater.* **4** 103609
[58] Methfessel M, Hennig D and Scheffler M 1992 *Phys. Rev.* B **46** 4816
[59] Tyson W and Miller W 1977 *Surf. Sci.* **62** 267
[60] Alexander R, Marinica M-C, Proville L, Willaime F, Arakawa K, Gilbert M R and Dudarev S L 2016 *Phys. Rev.* B **94** 024103
[61] Byggmästar J, Hamedani A, Nordlund K and Djurabekova F 2019 *Phys. Rev.* B **100** 144105
[62] Derlet P M, Nguyen-Manh D and Dudarev S L 2007 *Phys. Rev.* B **76** 054107
[63] Granberg F, Byggmästar J and Nordlund K 2020 *J. Nucl. Mater.* **528** 151843
[64] Yi X, Sand A E, Mason D R, Kirk M A, Roberts S G, Nordlund K and Dudarev S L 2015 *Europhys. Lett.* **110** 36001
[65] Miiller A and Cezairliyan A 1990 *Int. J. Thermophys.* **11** 619–28
[66] Dubrovinsky L and Saxena S 1997 *Phys. Chem. Miner.* **24** 547
[67] Ghaly M, Nordlund K and Averback R S 1999 *Phil. Mag.* A **79** 795
[68] Nordlund K, Ghaly M, Averback R S, Caturla M, Diaz de la Rubia T and Tarus J 1998 *Phys. Rev.* B **57** 7556
[69] Morris J R, Wang C Z, Ho K M and Chan C T 1994 *Phys. Rev.* B **49** 3109
[70] Schober H R and Dederichs P H 1981 *Phonon States of Elements. Electron States and Fermi Surfaces of Alloys—W* ed K-H Hellwege and J L Olsen (Springer)
[71] Kittel C 2005 *Introduction to Solid State Physics* 8th edn (Wiley)
[72] Becquart C, Domain C, Sarkar U, De Backer A and Hou M 2010 *J. Nucl. Mater.* **403** 75
[73] Fernandez N, Ferro Y and Kato D 2015 *Acta Mater.* **94** 307
[74] Heinola K and Ahlgren T 2010 *J. Appl. Phys.* **107** 113531
[75] Liu Y-L, Zhang Y, Luo G and Lu G-H 2009 *J. Nucl. Mater.* **390-391** 1032
[76] Heinola K, Ahlgren T, Nordlund K and Keinonen J 2010 *Phys. Rev.* B **82** 094102
[77] Johnson D and Carter E 2010 *J. Mater. Res* **25** 315
[78] Kresse G and Hafner J 1993 *Phys. Rev.* B **47** 558

[79] Kresse G and Furthmüller J 1996 *Phys. Rev.* B **54** 11169
[80] Kresse G and Furthmüller J 1996 *Comput. Mater. Sci.* **6** 15
[81] Nguyen-Manh D, Horsfield A P and Dudarev S 2006 *Phys. Rev.* B **73** 020101
[82] Nguyen-Manh D, Lavrentiev M Y, Muzyk M and Dudarev S L 2012 *J. Mater. Sci.* **47** 7385
[83] Perdew J P, Burke K and Ernzerhof M 1996 *Phys. Rev. Lett.* **77** 3865
[84] Heinola K and Ahlgren T 2010 *Phys. Rev.* B **81** 073409
[85] Ohsawa K and Kuramoto E 2007 *J. Nucl. Mater.* **367-370** 327
[86] Jenkins M and Kirk M 2001 *Characterization of Radiation Damage by Transmission Electron Microscopy* (*Microscopy in Materials Science*) (IOP)
[87] Dudarev S and Sutton A 2017 *Acta Mater.* **125** 425
[88] Stukowski A 2009 *Modelling Simul. Mater. Sci. Eng.* **18** 015012
[89] Stukowski A 2012 *Modelling Simul. Mater. Sci. Eng.* **20** 045021